

SPACE-BASED OPTICAL DETECTION SENSITIVITY TO ORBITAL CONFIGURATION, INSTRUMENT AND SIGNAL PROCESSING

Hugo Veuillez and Johan Montel

Department of Flight Dynamics, Centre National d'Etudes Spatiales (CNES), Toulouse, France, Email: hugo.veuillez@cnes.fr

ABSTRACT

This paper presents a system-level simulation tool designed to assess the performance of optical Space-Based Space Surveillance (SBSS) missions in detecting and characterizing new object orbits in Low Earth Orbit (LEO). The tool integrates comprehensive models for space population distribution, observer orbit and instrument characteristics (including signal and noise models), and detection methodologies. Through sensitivity analyses, we demonstrate how various parameters influence mission performance and highlight that mission optimization depends on whether the focus is on detecting small, ground-elusive objects, maximizing detection counts, or enhancing orbit determination accuracy. Our findings indicate that the full potential of optical instruments is currently underutilized due to constrained on-board computational resources or down-link capacities.

Keywords: SBSS; Optical Detection; Signal Model; Noise Model; SNR.

1. INTRODUCTION

The increasing population of satellites in Low Earth Orbit (LEO) necessitates advanced detection and tracking systems to minimize collision avoidance maneuvers. Optical tracking, being a passive method, is particularly effective for monitoring debris. Additionally, the need for enhanced detectability and increased measurement refresh rates makes embedded optical measurements increasingly attractive.

However, designing such an embedded system involves a multitude of parameters, making it challenging for simple order-of-magnitude models. Therefore, it is beneficial to develop simulation tools to ensure proper system dimensioning and validate mission concepts.

This paper presents a system-level simulation tool that quantifies the benefits of an optical Space-Based Space Surveillance (SBSS) mission. We describe the various models, assumptions, and techniques used in this simula-

tor. Finally, we present sensitivity results to demonstrate the impact of certain parameters on mission performance.

Note that the emphasis was placed on the system's ability to passively detect and characterize new object orbits, rather than tracking and improving specific known target orbits, which can be seen as a specific case of the former.

2. SPACE POPULATION

The first step for our simulator is to have a representative space object population. Most space agencies maintain a catalog of observable objects, with a typical minimum size of 10 cm. However, to evaluate the capability of a mission to detect smaller objects, it is necessary to have a statistically representative population of smaller objects.

One approach to achieve this goal is to simulate the evolution of a population by incorporating collision and fragmentation models, along with atmospheric re-entry models. After a few years of evolution, a population of smaller objects starts to appear, and its distribution is likely to be representative of the actual distribution of smaller objects [1][2].

We accessed one of these simulated populations generated by the European Space Agency (ESA) and used in Inter-Agency Space Debris Coordination Committee (IADC) studies, providing a distribution of objects down to 1 cm.

Fig. 1 illustrates that the debris density is proportional to $D^{-2.6}$, where D represents the debris equivalent diameter. This empirical relationship holds for both observed objects (> 10 cm) and simulated objects (< 10 cm), reinforcing our confidence in the simulation's ability to statistically represent the real population distribution for objects smaller than 10 cm. Furthermore, it underscores the presence of a significant quantity of debris that remains untracked by space agencies' catalogs, with approximately 400 times more objects of 1 cm than objects of 10 cm.

The analysis of this population's distribution also teaches us that even though circular polar orbits are more rep-

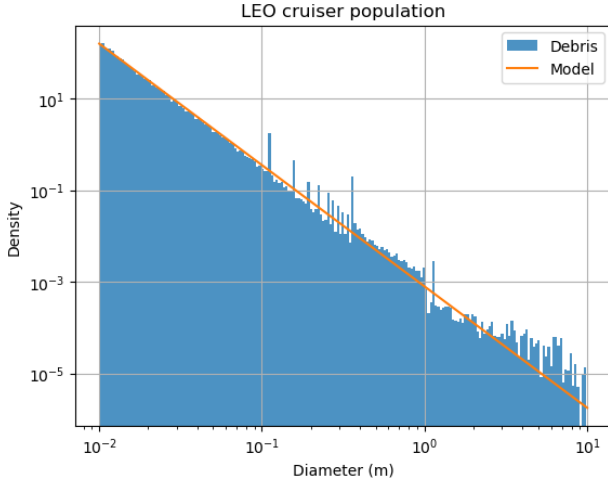


Figure 1. Debris density function (from ESA population) with respect to their diameter.

resented, they do not constitute the majority of debris. Additionally, the debris are homogeneously distributed in latitude, leading to a greater density around the poles¹.

Thereafter, a Kepler model is used to propagate the population (reasonable considering the short time scale, a few days, of the propagation).

3. OBSERVER'S CHARACTERISTICS

An optical SBSS system can contain several observers. In the following, we will focus on a single observer, but the concepts can be easily extended to multiple observers.

This section presents the various characteristics of our system, specifically the space component. The observer is characterized by its orbit, mission programming, and optical instrument.

3.1. Orbit

The observer is assumed to follow Keplerian motion. The software does not impose any constraints on the orbit. However, considering the highest object density is encountered at the poles, we opted for a circular and polar orbit in our usage of the software.

3.2. Mission programming

A key aspect of the system is determining when and where the observer should take images. Constraints may arise from on-board processing capacities, glare, telemetry/telecommand (TM/TC) slots, etc. Although

¹The available volume for a given latitude angle is smaller at the poles than at the equator, while the density per latitude is constant.

our software can accommodate any attitude and image sequences, we chose to restrict our usage to a fixed attitude in the local orbital frame of the observer and an image sequence regularly distributed over time.

Note that images can be considered mono or multi-frame depending on the detection method used. This will be discussed in Sec. 5.1.

3.3. Optical instrument

This section defines the vocabulary and components of the optical instrument used in our software.

3.3.1. Optical objective

The optical objective is the optical component of the instrument. It focuses light onto a focal plane and can be characterized by the following values:

- The optics diameter Φ . This is directly linked to the quantity of photons the optical instrument can capture. The optics surface S_{optics} can be expressed under a circular assumption as: $S_{optics} = \frac{\pi}{4}\Phi^2$.
- The focal length f . Combined with the lens diameter, this value defines the f-number $f_n = \frac{f}{\Phi}$, representing the optics aperture.
- The Point Spread Function (PSF). This function represents the optical response of a point source. In this article, a Gaussian PSF is considered:

$$PSF(x, y) = \frac{1}{2\pi\sigma_{PSF}^2} \exp\left(-\frac{x^2 + y^2}{2\sigma_{PSF}^2}\right) \quad (1)$$

where σ_{PSF} is the PSF width (see Appendix A.1 for notations). Note that x , y and σ_{PSF} are expressed in pixel.

3.3.2. Image Sensor

The image sensor converts light into a numerical signal and is positioned on the optical instrument's focal plane. It is characterized by the following values:

- The pixel size p (also called the pitch). The pixel shape is considered to be square in this article.
- The number of pixels in a line (or column) n_{lp} .
- The quantum efficiency $\rho_{quantic}$. This measures the sensor's efficiency in converting photons into electrons. A 50% efficiency means that 2 photons are necessary to generate 1 electron.

From these defined values, a few derived characteristics are interesting to note:

- The sensor size $D = n_l p$.
- The field of view² $\text{fov} = 2 \arctan\left(\frac{D}{2f}\right)$.
- The pixel field of view $\alpha_p = \frac{p}{f}$.

The optical sensor wavelength sensitivity domain Λ is defined as follows:

$$\Lambda = [\lambda_0 - \Delta\lambda/2, \lambda_0 + \Delta\lambda/2] \quad (2)$$

where λ_0 is the central wavelength, and $\Delta\lambda$ is the bandwidth. The bandwidth is assumed to be sufficiently narrow to consider that all spectral functions are constant over that range. For example, the silicon sensors considered in our simulation only work in the visible domain ([400, 800] nm).

4. IMAGING MODELS

In this section, the measured quantities will be expressed in terms of electrons, as this is the physical quantity closest to the actual measurement.

An image is composed of both useful and parasitic signals. The useful signal refers to the electrons generated by the target's photons, while parasitic electrons are generated by various other sources.

To detect a target with a certain level of confidence, we need the Signal-to-Noise Ratio (SNR) to be sufficiently high. In this section, we will present the different signals considered in our simulator and develop an expression to compute the SNR (depending on the detection method).

Throughout this section, we will denote t_i as the integration time of an individual image. All expressions will be relative to a single pixel.

4.1. Parasitic signal models

4.1.1. Readout noise

Readout noise is generated by the sensor electronics during the readout process. It is often provided by the sensor manufacturer as a standard deviation, expressed in terms of the number of electrons σ_{read} .

²The field of view is considered circular in this paper, even though sensors are usually square, because the sensor's corners are typically discarded by image processing due to higher vignetting.

In this article, a pragmatic model, proportional to the pitch, was chosen to scale the noise to different detectors:

$$\sigma_{read}(p) = \frac{p}{p_{ref}} \sigma_{read}(p_{ref}) \quad (3)$$

4.1.2. Dark signal

The dark signal refers to the flux of electrons generated in the absence of light. We model this quantity to be proportional to the pixel surface area and the integration time:

$$S_{dark} = s_{dark} p^2 t_i \quad (4)$$

where s_{dark} is the dark signal flux, which depends, among other things, on the sensor's temperature.

The electron dark signal can be modeled as a Poisson distribution. Thus, the standard deviation of this signal can be expressed as:

$$\sigma_{dark} = \sqrt{S_{dark}} \quad (5)$$

4.1.3. Stray light

Stray light is diffuse light coming from the environment, such as the Milky Way, atmospheric radiation, sunlight reflection in the baffle, etc.

In this article, we assume that the stray light is isotropic³, making it suitable to express it as a flux per solid angle. It is usually expressed as a magnitude per solid angle.

Let m_{stray} be the magnitude (with respect to Vega) of the stray light flux per solid angle. The photon flux per solid angle can be expressed, using the Vega photon flux calculated in Appendix B, as follows:

$$\varphi_{stray} = \varphi_{Vega} 10^{-\frac{m_{stray}}{2.5}} \quad (6)$$

Typical magnitudes, expressed per arcsecond squared, in space are around 21, while on the ground they are between 17 and 19. This is one of the reasons space-based optical measurements look attractive, as the stray light is much less present in space (by a factor of 1/15).

Finally, the number of electrons generated by the stray light can be expressed as:

$$S_{stray} = \rho_{quantic} \varphi_{stray} S_{optics} \alpha_p^2 t_i \quad (7)$$

where $\rho_{quantic}$ is the quantum efficiency, S_{optics} is the surface area of the optical instrument, α_p^2 is the pixel solid angle (all defined in Sec. 3.3.2), and t_i is the integration time.

³This is a significant simplification, as the Milky Way and the atmosphere are not isotropic. This hypothesis is to keep in mind, especially when the camera has the atmosphere in its field of view.

The electron stray signal can also be modeled as a Poisson distribution. Thus, the standard deviation of this signal can be expressed as:

$$\sigma_{stray} = \sqrt{S_{stray}} \quad (8)$$

4.1.4. Non-uniformities

Each pixel of the sensor has its own response "bias" that can be considered constant over the timescale of several images. These biases include Fixed Pattern Noise (FPN), Dark Signal Non-Uniformities (DSNU), spikes, etc.

These defects can be either calibrated or evaluated and corrected within the detection processing in the case of multi-frame image acquisition. For this reason, we will neglect these effects in the performance evaluation software.

4.1.5. Stars

The number of stars present in the optical field of view, whose signal is higher than the faintest detected object, increases exponentially with the sensitivity of the system. If not well addressed, these stars may become the major limitation of the detection capability.

If the observer maintains an inertial attitude during the observation, the stars will appear motionless in the images and will have the same signature as the non-uniformities. It will be possible to remove them with good efficiency using relatively simple techniques in the case of multi-frame images. However, if the pointing is not inertial, the stars will be spread across the image, forming streaks, and the problem will be more difficult to address.

Fourier transform techniques may be useful to remove both static defects in the sensor and inertial frames, but these techniques are not standard. It is also possible to use a star catalog to mask the pixels affected by predicted stars, although performing this correction for high magnitudes can be challenging.

Even though star pollution is not a trivial problem, it is a deterministic source of pollution. As with non-uniformities, we will consider in this study that this source of perturbation is perfectly corrected and has no major impact on the detection capability.

4.1.6. Complete noise model

From the previous sections, we can derive an expression for the total noise for each pixel of an image, considering that all the noise sources are independent:

$$\sigma = \sqrt{\sigma_{read}^2 + \sigma_{dark}^2 + \sigma_{stray}^2} \quad (9)$$

It can be convenient to highlight noise behavior with respect to the integration time. We can achieve this for the previous equation as follows:

$$\sigma = \sqrt{\eta + \zeta t_i} \quad (10)$$

where η represents the dominant noise contribution for low integration times (readout noise) and ζ represents the dominant noise contribution for high integration times (dark noise and stray light).

4.2. Useful signal model

4.2.1. Target signal

The signal received from the target is the result of sunlight reflection on the target. Typically, the reflection can be separated into diffuse and specular components [3] [4].

We consider here a simple spherical reflection model.

The diffuse component follows a Lambertian diffusion model. The proportion of reflected light reaching the observer, denoted as γ , can be expressed as:

$$\gamma = \frac{2}{3\pi} a_0(\lambda) \frac{d_0^2}{R^2} (\sin \theta + (\pi - \theta) \cos \theta) \quad (11)$$

where $a_0(\lambda)$ is the target reflectance at the given wavelength, d_0 is the target equivalent diameter, R is the distance between the target and the observer, and θ is the phase angle between the observer and the Sun, with respect to the target. The proportion of reflected light decreases with increasing phase angles.

Regarding the specular component, a spherical model is less likely to be representative of reality. Indeed, for any configuration, a perfect sphere always has a surface element that will produce a specular reflection towards the observer. However, for more complex geometries, a specular reflection only occurs at very specific orientations. For this reason, we neglect the specular contribution in our model.

Finally, the target signal can be expressed in terms of the number of electrons using the following equation:

$$S_{target} = \rho_{quantic} \gamma \varphi_{Sun} S_{optics} t_i = \psi_{target} t_i \quad (12)$$

where $\rho_{quantic}$ is the quantum efficiency, S_{optics} is the surface area of the optics, t_i is the integration time (all defined in Sec. 3.3.2), γ is the proportion of reflected sun's photon flux received by the observer, φ_{Sun} is the sun's photon flux, and ψ_{target} is the target photon flux.

However, this signal will be spread over several pixels, as explained in the next section.

4.2.2. Dynamic PSF

Because of the relative movement between the target and observer during the integration time, the target's image on the optical sensor is not simply given by the "static" PSF introduced in Sec. 3.3.1.

To describe the target's image, we first need to define the motion of the target in the optical sensor frame. Let's call \vec{v} the velocity vector of the target⁴ in that frame and \vec{u} the unit direction vector between the observer and the target.

The target motion \vec{d} on the sensor focal plane, in pixels, is given by:

$$\vec{d} = \frac{\vec{v} \perp \vec{u} t_i}{R \alpha_p} = \vec{\omega} t_i \quad (13)$$

where $\vec{v} \perp \vec{u}$ is the orthogonal component of \vec{v} with respect to \vec{u} , R is the distance between the target and the observer, t_i is the integration time, α_p is the angular size of a pixel, and ω is the pixel velocity.

We can now introduce the concept of dynamic PSF, which is the target's image during the integration time (see [5] for an equivalent introduction to this concept). It is the convolution (see Appendix A.3) of the "static" PSF, denoted here as PSF_{static} , with the motion of the target during the integration time:

$$PSF_{dyn} = PSF_{static} * \frac{1}{d} \Pi_{\vec{d}} \quad (14)$$

where $\Pi_{\vec{d}}$ is the 1D rectangle function of width and direction \vec{d} . An analytical expression of this equation can be found in Appendix C, under certain assumptions.

For the remainder of this article, we will omit the "dyn" suffix, but PSF will always refer to the dynamic PSF. Also note that all PSFs will be considered as unitary, meaning $\|PSF\|_1 = 1$ (see Appendix A.2 for norm definition).

For LEO observations, the relative angular velocity may be high, leading to a significant number of pixels being affected by the target motion. This results in the source signal being highly spread, forming long linear streaks on the image. Consequently, the useful signal is highly diluted in the noise, increasing the difficulty of its detection, as we will see.

5. PROCESSING

Once images are produced on board, they need to be processed. This process can be divided into two main steps:

1. Image processing to detect and extract observation directions.

⁴Note that \vec{v} is the composition of the relative inertial velocity with respect to the observer, composed with the observer rotation rate.

2. Orbit determination to convert direction data into orbits.

The first step involves significant data compression. After extracting observation directions, the original images can be discarded, reducing the data from millions of pixels to a few directional components. Performing this processing on-board significantly reduces the constraints on the link budget and may even allow for an increased number of images, although it requires higher on-board computational capacity.

In contrast, the second step offers little benefit from being performed on board. The compression level is much lower, and the availability of extensive population catalogs on the ground aids in associating detections with known objects.

5.1. Detection methods

The primary goal of a detection process is to identify a useful signal amidst noise in a single or multi-frame image.

The general methodology involves applying a transformation (linear or non-linear) to the raw image. This transformation produces a new single-frame image on which the detection process is performed. A detection occurs when a pixel's signal exceeds the noise by a predefined factor. For instance, in our simulation, we consider a detection when the SNR is above 5, indicating high confidence in the detection.

This section presents several detection methods and evaluates their theoretical SNR to quantify their efficiency.

To evaluate the SNR of each method, consider the detection of a unique object in a single-frame image, represented by the matrix Y . The intensity of the object's signal is denoted by the scalar s (see Equ. 12) and is spread around the pixel (i_0, j_0) by its dynamic PSF (see Equ. 14), represented⁵ by the matrix F . Note that the PSF function is unitary, so $\|F\|_1 = 1$. Additionally, let the image noise be represented by the matrix ϵ , where each component is an independent random variable with a standard deviation σ (see Equ. 9). The image can be represented as:

$$Y = Fs + \epsilon \quad (15)$$

5.1.1. Obvious detection

This method is applied to single-frame images and does not involve any transformation phase. The detection is performed directly on the raw image.

⁵The matrix F represents the PSF centered on the pixel (i_0, j_0) , but it is omitted in the notation for readability.

Each pixel is evaluated independently, and the pixel with the maximum object signal is chosen to compute the SNR. This results in the following expression:

$$SNR = \frac{\max(F)s}{\sigma} = \frac{\|PSF\|_{\infty}s}{\sigma} \quad (16)$$

This method can lead to a significant loss of signal. The more the input signal is spread across different pixels, the less signal is utilized by the obvious detection method.

Appendix C.1 provides a simplified expression for $\|PSF\|_{\infty}$. From this, we can deduce the asymptotic behavior of the SNR with respect to the integration time t_i :

$$\lim_{t_i \rightarrow 0} SNR \propto t_i \text{ and, } \lim_{t_i \rightarrow \infty} SNR \propto \frac{1}{\sqrt{t_i}} \quad (17)$$

This method therefore has an optimal integration time that depends on the target's angular velocity⁶.

5.1.2. Mono-frame image PSF convolution

An intuitive solution to improve the previous method is to consider a transformation that gathers all the signal of the object onto a single pixel. This operation is commonly used in image processing and is known as the convolution product.

Mathematically, this method can be introduced by considering the best linear estimator of the signal s . This can be found by solving the following least squares problem:

$$\min_s \|Y - Fs\|^2 \quad (18)$$

The solution to this problem is:

$$\hat{s} = \frac{\sum_{ij} F_{ij} Y_{ij}}{\sum_{ij} F_{ij}^2} \quad (19)$$

This solution is optimal for measuring the source signal at pixel (i_0, j_0) . However, in the detection framework, we do not know which pixel is concerned. The idea is to apply this transformation to every pixel, which is exactly a convolution operation with a kernel matrix representing the dynamic PSF. This technique is sometimes called "match filter" in the literature, see [6] for another demonstration.

The new image, on which the final detection phase is performed, can be defined as:

$$Y_c = \frac{PSF \star Y}{\|PSF\|_2^2} \quad (20)$$

⁶This optimum is the solution of a third-order polynomial, however it is quite intuitive that the order of magnitude of this optimum is the time required for the static PSF to pass over a pixel. Beyond this time, no more signal is dropped on the pixel while the noise still increases with time.

where PSF is the kernel matrix representing the dynamic PSF, and \star is the cross-correlation product (defined in Appendix A.3) instead of the convolution product, to apply correctly the PSF kernel. Note that this distinction is only necessary when the PSF is not symmetrical.

On average, pixels with a source signal will result in their own signal while their neighbor pixels will only have a portion of the signal. Other pixels will result in zero signal.

The least squares formalism also provides the variance of the signal estimator:

$$\text{var}(\hat{s}) = \frac{\sigma^2}{\|PSF\|_2^2} \quad (21)$$

We can now represent the SNR with the following equation:

$$SNR = \frac{s\|PSF\|_2}{\sigma} \quad (22)$$

Appendix C.2 provides a simplified expression for $\|PSF\|_2$. From this, we can deduce the asymptotic behavior of the SNR with respect to the integration time t_i :

$$\lim_{t_i \rightarrow 0} SNR \propto t_i \text{ and, } \lim_{t_i \rightarrow \infty} SNR \propto z \quad (23)$$

For this method, the SNR increases with t_i until reaching an asymptotic value. From Equ. 12, 55, 13 and 10, we have:

$$z = \frac{\psi_{target}}{\sqrt{2\pi\sigma_{PSF}\sqrt{\omega\zeta}}} \quad (24)$$

Now that this method is presented, some remarks are necessary:

- The primary challenge of this technique is that the target's motion \vec{d} is required for processing the image but remains unknown. However, a viable solution is to execute the process for sampled motion values (d_x, d_y) within a specified range $[-d_m, d_m]^2$ and focus on the samples triggering a detection candidate.
- We have $\|PSF\|_2 \geq \|PSF\|_{\infty}$, thus this method is mathematically superior to the obvious method.

5.1.3. Multi-frame shifted-summation image and convolution

With the previous method, if we double the integration time, so does the noise. However, if we split the integration time into two image-frames, and then sum the frames' signals, the noise will only increase by a factor of the square root of two due to the uncorrelation of the noise between successive frames. It thus may be more interesting to acquire n frames of integration time t_i than one frame of integration time nt_i .

Suppose the target's movement \vec{d} from frame k to $k + 1$ is known and considered to be linear and constant over k . The idea would be to shift and superimpose the frames so that the target's image matches perfectly on each frame.

The best linear process is then to apply the convolution method from the previous section to the summed-shifted image Y_s :

$$Y_s = \sum_k Y_k * \delta_{-(k-1)\vec{d}} \quad (25)$$

where Y_k are all the image frames, and $\delta_{-(k-1)\vec{d}}$ is a displacement convolution kernel of direction $(k-1)\vec{d}$.

The SNR can then be expressed as:

$$SNR = \frac{s \|PSF\|_2 \sqrt{n}}{\sigma} \quad (26)$$

The SNR now also grows with the square root of the number of image frames.

When $T_i = nt_i$ is fixed, it turns out that there is an optimal t_i to maximize the SNR. This optimal t_i tells us how many frames should be used for the image. It can be expressed as:

$$t_i^{opt} = \sqrt[3]{t_{rad} t_{geo}^2} \quad (27)$$

where

$t_{rad} = \frac{\eta}{\zeta}$ (see Equ. 10) represents the integration time for which time-dependent noises equal time-independent noises.

$t_{geo} = \frac{2\sqrt{\pi}\sigma_{PSF}}{\omega}$ (see Equ. 13 and 53) represents the integration time for which the streak length d (see Equ. 13) equals the inverse of the static PSF.

Once more, the target's motion \vec{d} is required for processing the image but remains unknown. The same brute force approach as for the previous method can be proposed. Clearly, it demands significant computational power, which may exceed on-board capabilities. Nevertheless, it is entirely feasible with ground-based computational resources, thereby shifting the issue to down-link capacities.

5.1.4. Other methods

A variety of other methods exist (see [5][6] for references). We highlight two detection methods found in the literature here.

Radon transform To reduce computational demands, it is possible to perform summations not for all displacements (d_x, d_y) , but only along segments that completely traverse a single image (referred to below as "full crossing segments"), see [6]. The trade-offs include:

- A loss in SNR, which can be quantified, to a first-order approximation, as the square root of the ratio of the full crossing segment's length to the actual object streak's length.
- The applicability to single-frame images only. However, single-frame images can first be computed from multi-frame images using non-linear methods such as max or max-med techniques (see below).

Non-linear methods Non-linear methods often involve algorithms or filters that use non-linear operators such as thresholds, max, min, median, and other non-linear conditions to filter or select pixels or regions of potential interest in images. The primary advantage of these algorithms is their computational efficiency, making them well-suited for on-board implementation or for compressing images to download for ground-based analysis.

An example is the "max" or "max minus median" operator, which compresses a series of multi-frame images into a single-frame resulting image. The result image is composed, for each pixel (i, j) , of the max or max-median signal of pixel (i, j) in each frame. This operation removes the non-uniformity (NU) of the pixel (i, j) through median subtraction and captures the object's signal when it crosses the pixel (i, j) , with noise equivalent to that of a single image. The resulting image can then be processed to detect streaks.

The main drawback of such methods is a loss of efficiency for low signal levels relative to the noise. Indeed, we can easily understand that when the signal is close to or below the noise level, the max pixel is less likely to correspond to the frame's pixel containing the signal. We can highlight this reasoning with a simulation. Let's compute the signal expected value of a 5-frame image's pixel for the max or max-median methods. Fig. 2 shows the output signal for each method when one of the 5 pixels is lit by an input signal (normalized with respect to the noise)⁷. We can see that the output signal is non-linear with respect to the input⁸, especially when the input signal is close to or below the noise, which is where we want the methods to be as efficient as possible.

5.2. Orbit determination accuracy

If no prior information about the object is available, it is first necessary to perform an Initial Orbit Determination (IOD). For direction measurements, several algorithms exist (Laplace, Gauss, Gibbs, etc.). However, they all require at least three successive observations [7, §7.3][8].

⁷For example, if a pixel receives a 2-SNR signal, on average, the output signal will only be 1-SNR for the max method. Indeed, in many cases, the max pixel is different from the pixel containing the signal, resulting in a 0-SNR.

⁸One can show that the slope, in zero, of these functions is $1/n$ for the max method, where n is the number of frames and zero for the max-median method.

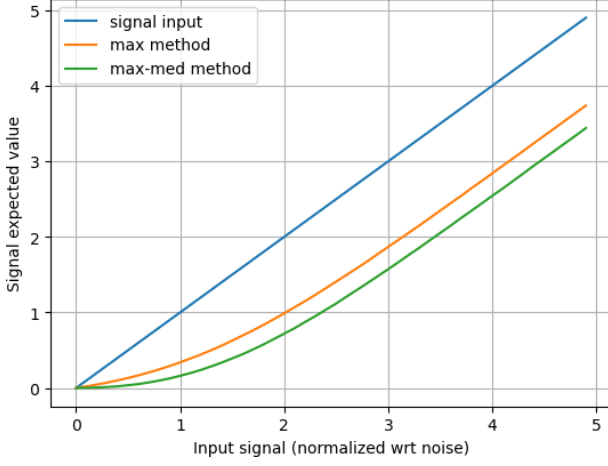


Figure 2. Max and Max-median method efficiency for 5 frames.

Once the IOD provides a rough orbit estimate based on simplified hypotheses, a more refined Orbit Determination (OD) can be performed using more sophisticated models. The OD is often carried out with a least squares filter, which provides an estimate of the solution error [9, §4 and §6].

In our software, we use this error estimation to perform what is often called a "covariance analysis" to assess the efficiency of a SBSS system in detecting and characterizing new objects.

The first challenge is to associate three successive observations to a single object. This can be achieved through an estimation of the object's velocity in the focal plane. This velocity estimation can be obtained, for example, from the streak length and orientation on a single-frame image or as a direct output of the summation method (Sec. 5.1.3). Using this velocity, an extrapolation between successive observations can be performed to determine if they correspond to the same object. Although this step may lead to incorrect associations, we considered it sufficiently reliable in our simulations to ignore these particular cases.

The second challenge is that IOD methods are not perfectly reliable and may struggle to converge. This aspect was neglected in our simulations, where we focused solely on the covariance analysis.

Finally, the third challenge is to model the precision of the direction extracted from the detection method. This input is necessary to assess the precision of the OD orbit. To detect the position of the target, a centroiding method is used. It consists of applying a weighted barycenter on the pixels affected by the signal.

Classical centroiding The most simple centroiding method consists in using the pixels' amplitude as weights. Let's model the intensity of a pixel with the following

equation:

$$v_{ij} = s_{ij} + \epsilon_{ij} \quad (28)$$

where v_{ij} is the total intensity, s_{ij} is the signal intensity and ϵ_{ij} is the noise intensity of the pixel (i, j) . The noise is considered independent between pixels, with a standard deviation σ . The position (p_x, p_y) of the target is then calculated as:

$$p_x = \frac{\sum_{i \in \mathcal{J}_x} \sum_{j \in \mathcal{J}_y} i v_{ij}}{\sum_{(i,j) \in (\mathcal{J}_x \otimes \mathcal{J}_y)} v_{ij}} \quad (29)$$

$$p_y = \frac{\sum_{i \in \mathcal{J}_x} \sum_{j \in \mathcal{J}_y} j v_{ij}}{\sum_{(i,j) \in (\mathcal{J}_x \otimes \mathcal{J}_y)} v_{ij}} \quad (30)$$

where $\mathcal{J}_x = [-N_x/2, N_x/2]$ and $\mathcal{J}_y = [-N_y/2, N_y/2]$ represent the domains, in x and y directions, around the streak's central pixel. The variance of the position can be expressed as:

$$\text{var}(p_x) = \frac{\sigma^2 N_y N_x (N_x - 1)(N_x + 1)}{s^2 12} \quad (31)$$

$$\text{var}(p_y) = \frac{\sigma^2 N_x N_y (N_y - 1)(N_y + 1)}{s^2 12} \quad (32)$$

where $s = \sum_{ij} s_{ij} \sim \sum_{ij} y_{ij}$, and can be expressed with respect to the SNR using the SNR expression of the chosen method.

Let's assume the velocity is along the x -axis, and we consider a margin of 3 static PSF on each side of the streak, we have $N_x = d + 6\sigma_{PSF}$ (where d is defined in Equ. 13), and $N_y = 6\sigma_{PSF}$. Using Equ. 22, with asymptotic Equ. 55, we can deduce the following uncertainties:

$$\sigma_{p_x} \sim \frac{(d + 6\sigma_{PSF})^{3/2}}{2 \text{SNR} (\pi d^2 + 4\pi^2 \sigma_{PSF}^2)^{1/4}} \quad (33)$$

$$\sigma_{p_y} \sim \frac{3\sqrt{3}\sigma_{PSF}}{\sqrt{\pi} \text{SNR}} \quad (34)$$

Optimal centroiding The previous method is not optimal since it does not take into consideration the a priori distribution of the signal on the sensor. A better weighting is possible by solving the following least square problem:

$$\min_{\vec{p}} \|Y - (F * \delta_{\vec{p} - \vec{p}_0})s\|^2 \quad (35)$$

where Y is the image, s is the signal centered on the pixel \vec{p}_0 , F is the PSF matrix centered on \vec{p}_0 and $(F * \delta_{\vec{p} - \vec{p}_0})$ is the PSF matrix centered on \vec{p} .

In the linear domain, the solution can be expressed as:

$$\delta \hat{p}_x = \frac{\sum_{ij} (F'_x)_{ij} [Y_{ij} - F_{ij}s]}{s \sum_{ij} (F'_x)_{ij}^2} \quad (36)$$

$$\delta \hat{p}_y = \frac{\sum_{ij} (F'_y)_{ij} [Y_{ij} - F_{ij}s]}{s \sum_{ij} (F'_y)_{ij}^2} \quad (37)$$

where $F'_x = \frac{\partial F}{\partial x}$ and $F'_y = \frac{\partial F}{\partial y}$

The variance of the solution is expressed as:

$$\text{var}(\delta\hat{p}_x) = \frac{\sigma^2}{s^2 \|PSF'_x\|_2^2} \quad (38)$$

$$\text{var}(\delta\hat{p}_y) = \frac{\sigma^2}{s^2 \|PSF'_y\|_2^2} \quad (39)$$

It is interesting to note that now, the weighting depends on the derivative of the PSF, meaning the pixels that have the most weight are the ones where the signal varies the most. Conversely, pixels where the signal does not vary significantly are less weighted, introducing significantly less noise to the centroiding solution.

It can be shown that the standard deviation along the x-axis grows with the square root of the streak's length for this method, whereas it grows linearly for the classical method.

6. SIMULATION SOFTWARE DESCRIPTION

Our simulation software was developed using PATRIUS, a CNES space dynamics library [10].

The software is separated into two distinct parts:

1. Simulate all possible detections for a given scenario. See Algorithm 1 for a pseudo-code description.
2. Analyze the simulated detections to apply a covariance analysis. The first goal is to identify the achievable orbit accuracy for one observation of at least 3 successive measurements. The second goal is to identify if the determined orbits are sufficiently accurate to recognize the detected object the next time it is detected.

Table 1 provides the physical values used in the simulation tool.

7. RESULTS

The primary goal of this article is to present our simulation software, its models, and detection techniques, as discussed in the previous sections.

This section presents a selection of relevant results and sensitivity analyses. Note that this cannot be exhaustive, as mentioned in the introduction, due to the numerous parameters and possible output representations involved in a complete sensitivity analysis.

All parameters used in the sensitivity analysis are detailed in Sec. 3. Various output representations can be of interest:

Algorithm 1: Simulator's pseudo-code

Input: dates = the observation dates
Input: population = the space population
Input: fov = the observer's field of view
Input: threshold = the SNR detection threshold
Output: The detection events with computed SNR

```

1 for date ∈ dates do
2   for target ∈ population do
3     if target ∈ fov then
4       snr ← computeSNR(target) ;
5       if snr > threshold then
6         | save(date, target, snr) ;
7       end
8     end
9   end
10 end

```

Name	Value	Reference
f_n	1.4	Sec. 3.3.1
$\rho_{quantic}$	0.5	Sec. 3.3.2
σ_{PSF}	0.8 pixel	Equ. 1
λ	0.6 μm	Equ. 2
$\Delta\lambda$	0.4 μm	Equ. 2
$\sigma_{read}(3.5 \mu m)$	2.5 e^-	Equ. 3
s_{dark}	0.8 $e^- / s / \mu m^2$	Equ. 4
m_{stray}	19 $arcsec^{-2}$	Equ. 6
a_0	0.1	Equ. 11
$\phi_{Sun}(0.55 \mu m)$	1850 $W/m^2 / \mu m$	Equ. 43
T_{Sun}	5777 K	Equ. 43
$\phi_{Vega}(0.55 \mu m)$	35.5 $nW/m^2 / \mu m$	Equ. 43
T_{Vega}	9600 K	Equ. 43

Table 1. Simulation numerical values

- Per image:
 - The number of detections (including repetitions of the same objects) with respect to different characteristics: size (Fig. 3), distance (Fig. 5), orbital position (Fig. 4), or detection methods.
 - The distribution of detected targets' direction or angular velocity (Fig. 6).
- Per day (or any other relevant duration):
 - The number of different detected objects.
 - The number of n successive detections (e.g., 3 or more to ensure IOD convergence) (Fig. 10).
 - The proportion of detected objects relative to those that passed within the observer's field of view.

7.1. Results with fixed input parameters

In this section, we present some of the listed outputs using a fixed set of parameters.

We use a sun-synchronous orbit at an altitude of 600 km , with a beta angle⁹ of approximately 70 degrees. The camera is tilted by 5 degrees below the observer’s velocity vector. An image is taken every 30 seconds. The integration time is 0.5 s , with 10 frames¹⁰ for the multi-frame detection method. The camera has an 85 mm diameter optical instrument and a detector of 10.5 mm with 3000 linear pixels (5° field of view). The simulation is performed for 1 day.

Our study focuses on objects smaller than 1 meter to emphasize the challenges in observing such objects.

Detection method efficiency This paragraph highlights the differences in efficiency among the detection methods.

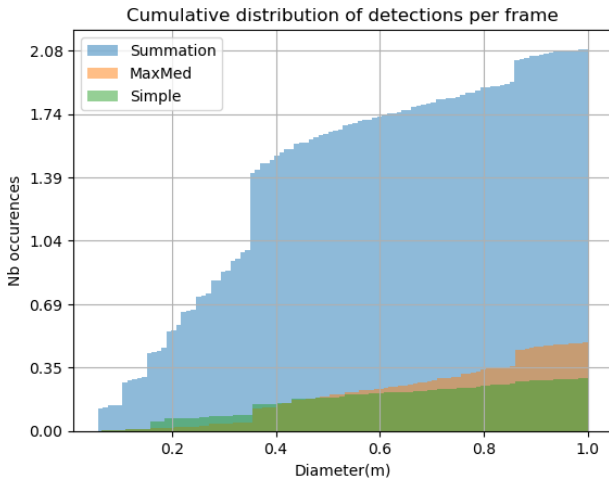


Figure 3. Comparison of different detection methods with respect to object’s size.

Fig. 3 shows the cumulative number of detections with respect to the object’s diameter for each method. Key observations include:

- On average, few objects are detected per image.
- The summation method is, on average, an order of magnitude more effective than the others.
- The max-med method’s inefficiency compared to the simple detection method at low SNR is visible.
- For very small objects (less than tens of centimeters), only the summation method is effective.

Other noteworthy outputs Fig. 4 shows a higher density of detections just before the poles (coordinates $\pm 90^\circ$), consistent with the higher density of objects at the poles (see Sec. 2) and the camera’s forward-looking.

⁹The angle between the orbital plane and the Sun.

¹⁰Each frame has an integration time of 0.05 s to compare methods with the same integration time.

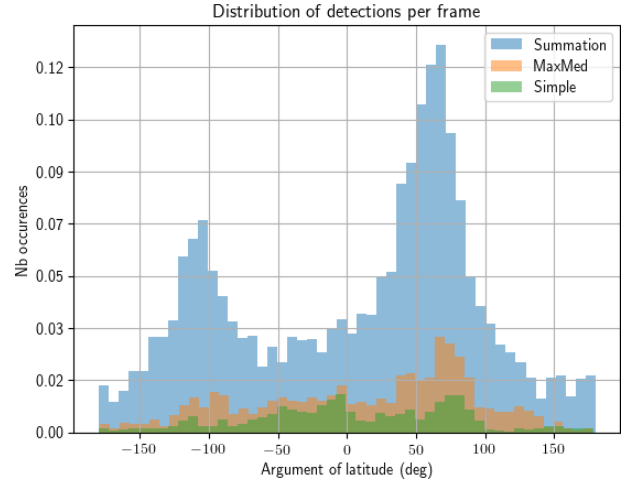


Figure 4. Comparison of different detection methods with respect to argument of latitude.

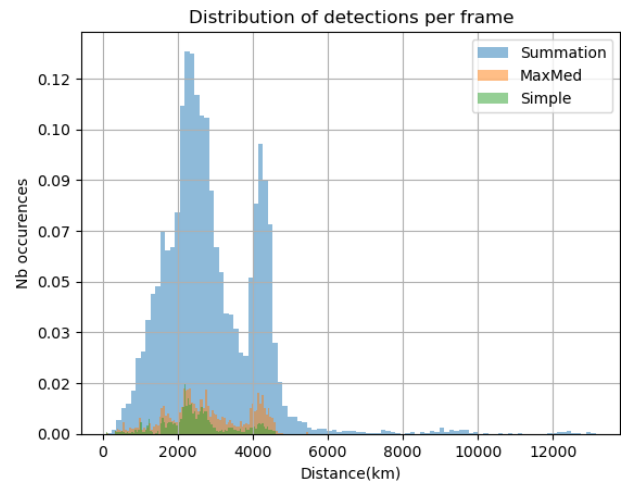


Figure 5. Comparison of different detection methods with respect to object’s distance.

Fig. 5 shows an optimal distance for detections. Closer objects have higher signal flux but also higher angular motion (thus signal is diluted in noise). Furthermore, fewer objects are within the field of view¹¹. Therefore, closer objects may be more difficult to detect, and their position accuracy may be degraded due to the increased length of their streaks.

Fig. 6 shows the different velocities to be tested in the shifted-summation brute force method.

¹¹The signal flux varies quadratically with distance (see Equ. 11), the angular motion varies linearly with distance (see Equ. 13), and the number of objects in the field of view at a given distance varies quadratically with distance.

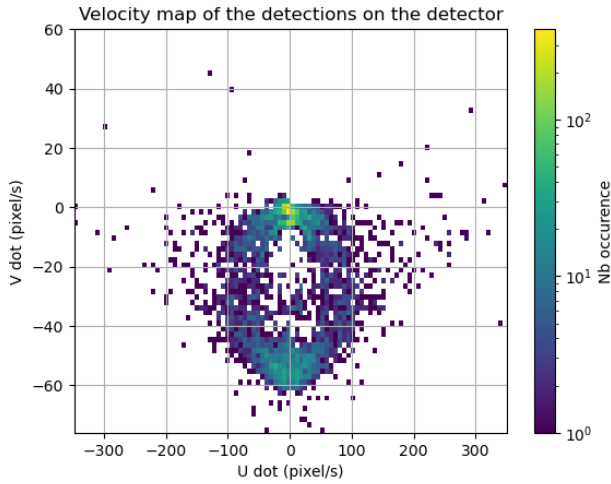


Figure 6. Velocity map of detections.

7.2. Sensitivity to input parameters

The design and optimization phase of an SBSS mission require sensitivity analysis. Our simulation software meets this need.

The following sections present a couple of sensitivity analyses, performed using the summation method, and with the same hypotheses as the previous section except for specific parameters for each section.

7.2.1. Orbit sensitivity

This section varies the altitude and the camera's pitch angle in Fig. 7 and the beta angle in Fig. 8.

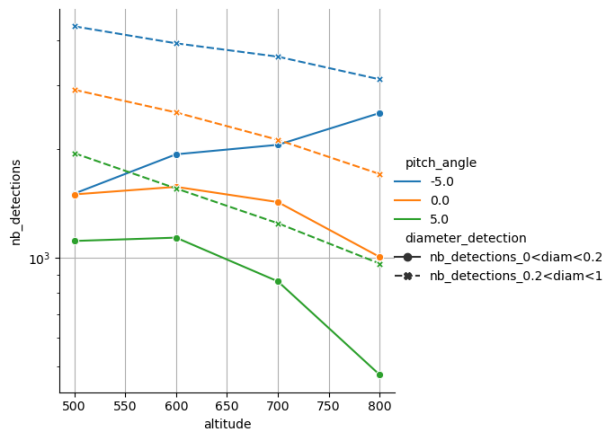


Figure 7. Sensitivity of the number of detections to altitude (km) and camera pitch angle (degrees).

Fig. 7 shows that the number of detections is maximized when the pitch is negative (the camera looks below the velocity direction). Beware that the atmosphere stray light is not considered here and might slightly change

the conclusion for wide fields of view. The altitude's impact depends on the object's size. It increases for small objects ($< 20 \text{ cm}$) while decreasing for larger objects ($> 20 \text{ cm}$).

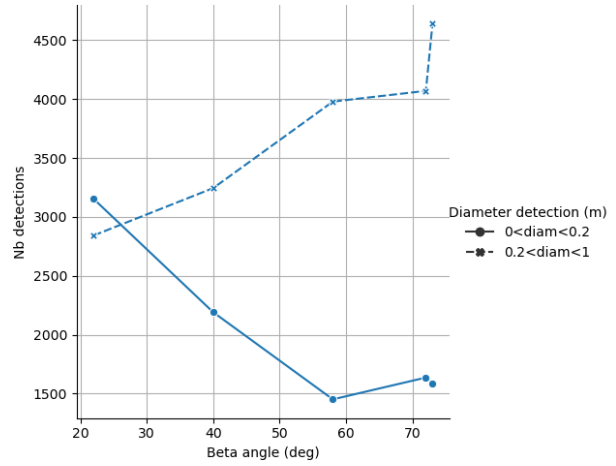


Figure 8. Sensitivity of the number of detections to the beta angle.

Fig. 8 shows that the optimal beta angle depends on the object category. For small objects, smaller beta angles are more advantageous to maximize the SNR during half of the orbit (to have a small sun phase angle, see Equ. 11), even though the other half of the orbit is unexploitable due to the unfavorable phase angle. For larger objects, a favorable phase angle throughout the entire orbit is preferable.

7.2.2. Optical sensitivity

The choice of the optical instrument significantly impacts mission efficiency.

This section compares the camera defined in Sec. 7.1, referred to as "large camera" with a smaller camera with a 34 mm diameter (12.5° field of view) and a 1000 linear pixel detector, referred to as "small camera".

Fig. 9 shows that the larger camera provides much higher detectability, except for the largest objects ($> 50 \text{ cm}$). For these bright objects, the camera's sensitivity is less critical, and wide field of view is more efficient.

Fig. 10 shows that very few triple successive detections occur¹². As a consequence, many detections are not usable for IOD and are only relevant when ground catalog association is possible. To increase the number of triple detections, two levers are possible: reduce the time between images but this will also reduce the geometric distribution of measurements (leading to an ill-conditioned problem), or increase the instrument's field of view, but this will reduce its sensitivity. The former is represented

¹²This observation is consistent across all detection methods, one had to be chosen for the plot.

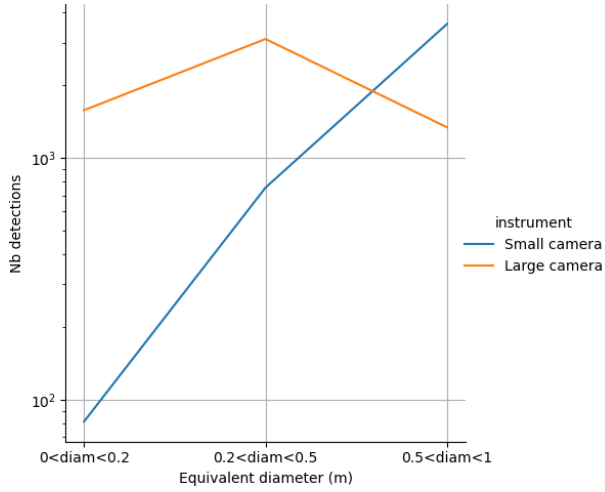


Figure 9. Sensitivity of the number of detections for 2 different instruments, for different object sizes.

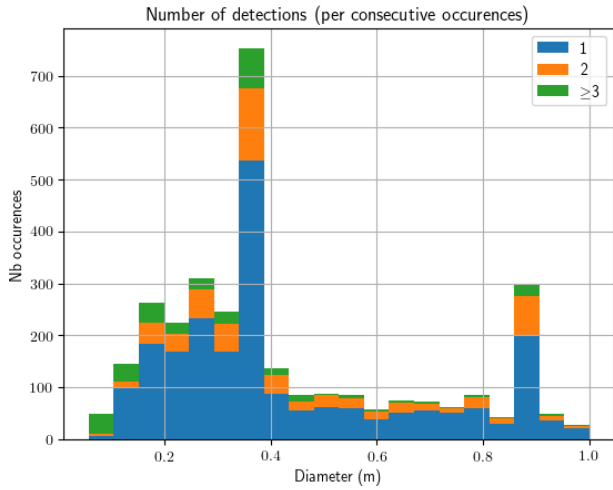


Figure 10. Number of detections (per consecutive occurrences) for the summation method, for images taken every 30 seconds, for instrument 1.

in Fig. 11. Instrument 1 generated 337 triple (or more) detections while instrument 2 generated 579.

7.3. Covariance analysis

In this section, the classical centroiding method (see Sec. 5.2) was used for simplicity. Note that using the optimal centroiding method, also presented in Sec. 5.2, can improve accuracy by a factor of 2 to 4, depending on the length of the streak.

In this section, we define a detection set as a set of successive observations of the same object. An object can be associated with several detection sets.

Figure 12 shows the orbit accuracy resulting from unique detection sets. The orbit accuracy is quite variable, rang-

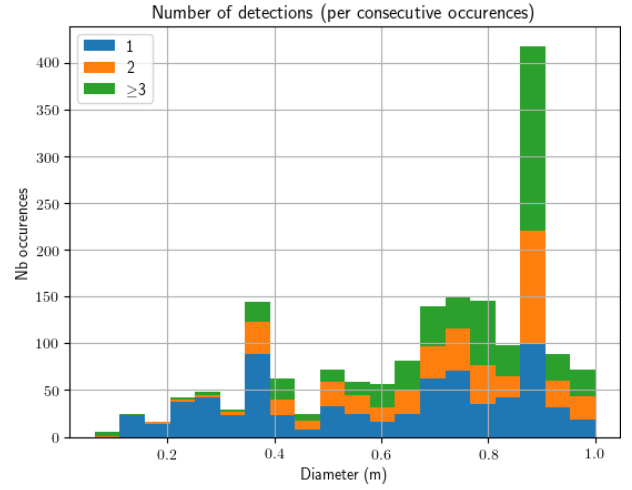


Figure 11. Number of detections (per consecutive occurrences) for the summation method, for images taken every 30 seconds, for instrument 2.

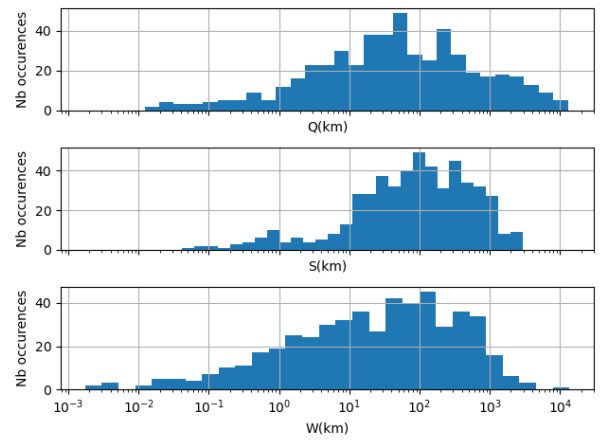


Figure 12. Orbit determination standard deviation in the local orbital frame (Q is along the radial vector, W is along the orbit momentum, and S completes the trihedron).

ing from a few kilometers to hundreds of kilometers.

Figure 13 shows the pixel uncertainty of an already characterized object at the date of a new detection set. It provides an indication of how difficult it might be to recognize the detected object from a previous characterization. The accuracy is quite variable and can go up to a thousand pixels. The association with previously characterized orbits is thus not always guaranteed.

8. CONCLUSION

This paper introduces a simulation tool designed to assess the effectiveness of optical space surveillance missions in identifying and tracking new objects in LEO. The tool

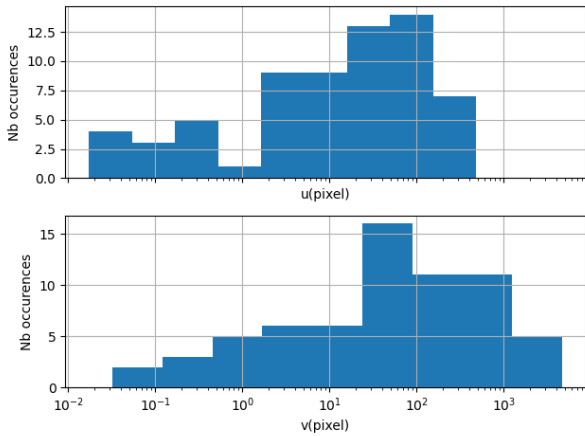


Figure 13. Pixel standard deviation for detection sets of previously characterized objects.

integrates detailed models for space population distribution, observer orbital and instrument characteristics, and detection methodologies, providing a robust framework for mission analysis.

Key findings from our sensitivity analyses include:

- The summation detection method outperforms other methods, particularly for small objects.
- Optimal detection conditions depends on the targeted objects size. Sensitivity and field of view are two opposite key points in the optimization of a mission.
- The number of successive detections, crucial for IOD, is significantly influenced by the time interval between images and the instrument's field of view.
- Orbit determination accuracy varies widely. In many cases, the accuracy is not sufficient to associate a tracked object to its next detection without other measurement sources.

These findings highlight the importance of tailoring mission parameters to specific objectives and show that the full capabilities of optical instruments are not fully exploited due to limitations in onboard processing and data transmission.

Future efforts will focus on enhancing the tool and validating it with real mission data to improve overall mission performance.

9. CONCLUSION

This paper presents a simulation tool designed to evaluate the effectiveness of optical space surveillance missions in identifying and tracking new objects in LEO. The tool

integrates detailed models for space population distribution, observer orbital and instrument characteristics, and detection methodologies, providing a robust framework for mission analysis.

Key findings from our sensitivity analyses include:

- The summation detection method outperforms other methods, particularly for small objects.
- Optimal detection conditions depend on the targeted object size. Sensitivity and field of view are two opposing key factors in mission optimization.
- The number of successive detections, crucial for initial orbit determination, is significantly influenced by the time interval between images and the instrument's field of view.
- Orbit determination accuracy varies widely. In many cases, the accuracy is insufficient to associate a previously tracked object with its next detection without additional measurement sources.

These findings underscore the importance of tailoring mission parameters to specific objectives and reveal that the full capabilities of optical instruments are not fully exploited due to limitations in onboard processing and data transmission.

Future efforts will focus on placing greater emphasis on the in-depth exploitation of the tool's capabilities and the establishment of more structured results. This will involve detailed analyses of various mission scenarios. Additionally, continuous efforts will be made to enhance the tool and validate it with real mission data to improve overall representativity. Finally, efforts are still dedicated to improving the onboard method's treatments to enhance the efficiency and profitability of the space based optical debris detection.

ACKNOWLEDGMENTS

The authors would like to express their gratitude to ESA space debris office for providing the debris population data used in this study.

The authors would like to thank "Le Chat", a virtual assistant powered by artificial intelligence, for its help in improving the readability, grammar, and language of this article.

APPENDIX

A. MATHEMATICAL DEFINITIONS

This appendix aims to define the mathematical objects used in this article.

A.1. Continuous versus discrete domain

Theoretical notions and models are easily defined in the continuous domain (Gaussian and rectangular functions, Fourier transform, Parseval equality, etc.), while the optical sensor, for which the mathematical objects should be applied, is composed of pixels and therefore is defined in the discrete domain.

In the continuous domain, the functions are defined on \mathbb{R}^2 . We call the coordinates x and y . In the discrete domain, the functions are defined on \mathcal{I}^2 where $\mathcal{I} = [0, n_{lp}]$, with n_{lp} defined in Sec. 3.3.2. We call the coordinates i and j .

The conversion of functions from continuous to discrete is not trivial. Formally, if we have a function f defined on \mathbb{R}^2 , its discrete equivalent is defined as:

$$F_{ij} = (f * \Pi)(i, j) \quad (40)$$

where $*$ is the convolution product (see Sec. A.3), and Π is the 2D rectangular function of a pixel size, centered on zero.

In this article, we consider that the pixels are sufficiently small to assume that the functions are constant over the pixel area¹³. Thus, to transform a function from continuous to discrete, we simply need to multiply the continuous function by the surface area of a pixel. By choosing pixel units, we simply have an equivalence between continuous and discrete function expressions.

The following sections are described in the continuous domain.

A.2. Norms

Let's denote f a function defined on \mathbb{R}^2 . We define L-norms as:

- The norm-1: $\|f\|_1 = \int_{xy} |f(x, y)| dx dy$
- The norm-2: $\|f\|_2 = \sqrt{\int_{xy} f^2(x, y) dx dy}$
- The norm-∞: $\|f\|_\infty = \max_{xy} (|f(x, y)|)$

A.3. Convolution and cross-correlation product

The convolution product $*$ is defined as:

$$(f * g)(x, y) = \int_{(t, \tau) \in \mathbb{R}^2} f(t, \tau) g(x - t, y - \tau) dt d\tau \quad (41)$$

¹³This assumption is quite strong and sometimes false, but for a simulation process, we consider it acceptable.

The cross-correlation product \star is defined as:

$$(f \star g)(x, y) = f(x, y) * g(-y, -x) \quad (42)$$

Note that both products respect Parseval's theorem.

B. STAR PHOTON FLUX IN OPTICAL SENSOR BANDWIDTH

The light emitted by a star can be modeled as a black body. Planck's law provides a relationship between the spectral energy fluxes $\phi(\lambda)$ at different wavelengths:

$$\phi_{star}(\lambda) = \phi_{star}(\lambda_{ref}) \left(\frac{\lambda_{ref}}{\lambda} \right)^5 \frac{\exp\left(\frac{hc}{\lambda_{ref} k_b T_s}\right) - 1}{\exp\left(\frac{hc}{\lambda k_b T_s}\right) - 1} \quad (43)$$

where λ is the wavelength, h is the Planck constant, c is the speed of light, k_b is the Boltzmann constant, and T_s is the surface temperature of the star.

To convert the spectral energy flux $\phi(\lambda)$ to the energy flux ϕ detected by the optical sensor, it is necessary to integrate over the sensor's sensitivity bandwidth. As explained in Sec. 3.3.2, the bandwidth is sufficiently narrow to consider the spectral energy flux as constant over that range. Thus, we have:

$$\phi_{star} = \int_{\lambda_0}^{\lambda_1} \phi_{star}(\lambda) d\lambda \approx \phi_{star}(\lambda_0) \Delta\lambda \quad (44)$$

where $\Delta\lambda = \lambda_1 - \lambda_0$ is the sensitivity bandwidth of the optical sensor.

Finally, for our study, it is convenient to convert the energy flux ϕ into a photon flux φ . To do this, we use the definition of the photon's energy:

$$E_{photon} = \frac{hc}{\lambda} \quad (45)$$

where h is the Planck constant, c is the speed of light, and λ is the photon's wavelength.

The photon flux can thus be expressed as:

$$\varphi = \frac{\lambda \phi_{star}}{hc} \quad (46)$$

C. EXPRESSION OF THE DYNAMIC PSF

Equ. 14 can be expressed analytically¹⁴ using the static PSF Eq. 1 and supposing, for simplicity, that the target

¹⁴The proof is not exposed here. However, the formula simply derives from the definition of the convolution and the error function (erf).

motion is only along the x-axis:

$$PSF_{dyn}(x, y) = \frac{1}{\sqrt{2\pi}\sigma_{PSF}} \exp\left(-\frac{y^2}{2\sigma_{PSF}^2}\right) \frac{1}{2d} \left[\operatorname{erf}\left(\frac{d-x}{\sqrt{2}\sigma_{PSF}}\right) + \operatorname{erf}\left(\frac{d+x}{\sqrt{2}\sigma_{PSF}}\right) \right] \quad (47)$$

where $\operatorname{erf}(x) = \frac{2}{\sqrt{\pi}} \int_0^x \exp(-t^2) dt$.

C.1. Norm- ∞

The norm- ∞ can be expressed as:

$$\begin{aligned} \|PSF_{dyn}\|_{\infty} &= PSF_{dyn}(0, 0) \\ &= \frac{1}{\sqrt{2\pi}\sigma_{PSF}d} \operatorname{erf}\left(\frac{d}{\sqrt{2}\sigma_{PSF}}\right) \end{aligned} \quad (48)$$

Asymptotically in $\delta = \frac{d}{\sigma_{PSF}}$, we have:

$$\lim_{\delta \rightarrow 0} \|PSF_{dyn}\|_{\infty} = \frac{1}{2\pi\sigma_{PSF}^2} = \|PSF_{static}\|_{\infty} \quad (49)$$

$$\lim_{\delta \rightarrow \infty} \|PSF_{dyn}\|_{\infty} = \frac{1}{\sqrt{2\pi}\sigma_{PSF}d} = \frac{\sqrt{\|PSF_{static}\|_{\infty}}}{d} \quad (50)$$

We can thus define an asymptotic formulation as:

$$\|PSF_{dyn}\|_{\infty} \sim \frac{\|PSF_{static}\|_{\infty}}{\sqrt{1 + d^2\|PSF_{static}\|_{\infty}}} \quad (51)$$

C.2. Norm-2

The norm-2 can be expressed as¹⁵:

$$\|PSF_{dyn}\|_2^2 = \frac{1}{\sqrt{\pi}d^2} \left(\frac{\exp(-\delta^2) - 1}{\sqrt{\pi}} + \delta \operatorname{erf}(\delta) \right) \quad (52)$$

where $\delta = \frac{d}{2\sigma_{PSF}}$. Asymptotically in δ , we have:

$$\lim_{\delta \rightarrow 0} \|PSF_{dyn}\|_2^2 = \frac{1}{4\pi\sigma_{PSF}^2} = \|PSF_{static}\|_2^2 \quad (53)$$

¹⁵The proof is not exposed here because of page limitations, even though it is not trivial. A few steps can be quickly provided though. Start again from Equ. 14. The Parseval norm equality allows us to compute the norm in the Fourier domain to transform the convolution into a simple product (the rectangle function transforms to a sinc function). Then, some manipulations on the integral are required: derive three times to find a differential relation of the integral to its second derivative. Perform some variable changes, by parts integrations, and finally handle the normalization factors correctly.

$$\lim_{\delta \rightarrow \infty} \|PSF_{dyn}\|_2^2 = \frac{1}{2\sqrt{\pi}\sigma_{PSF}d} = \frac{\|PSF_{static}\|_2}{d} \quad (54)$$

We can thus define an asymptotic formulation as:

$$\|PSF_{dyn}\|_2^2 \sim \frac{\|PSF_{static}\|_2}{\sqrt{d^2 + \|PSF_{static}\|_2^{-2}}} \quad (55)$$

REFERENCES

1. H Klinkrad, J Bendisch, KD Bunte, H Krag, H Sdunus, and P Wegener. The master-99 space debris and meteoroid environment model. *Advances in Space Research*, 28(9):1355–1366, 2001.
2. DOLADO-PEREZ Jc, D Romain, and REVELIN Bruno. Introducing medee—a new orbital debris evolutionary model. In *Proceeding of the 6th European Conference on Space Debris*, 2013.
3. Eugene Michael Vallerie and USAF CAPT III. *Investigation of photometric data received from an artificial earth satellite*. PhD thesis, Air Force Institute of Technology, 1963.
4. William Eric Krag. Visible magnitude of typical satellites in synchronous orbits. *NASA STI/Recon Technical Report N, 75:12024*, 1974.
5. Bin Lin, Lijun Zhong, Sheng Zhuge, Xia Yang, Yang Yang, Kunpeng Wang, and Xiaohu Zhang. A new pattern for detection of streak-like space target from single optical images. *IEEE Transactions on Geoscience and Remote Sensing*, 60:1–13, 2021.
6. Guy Nir, Barak Zackay, and Eran O Ofek. Optimal and efficient streak detection in astronomical images. *The Astronomical Journal*, 156(5):229, 2018.
7. David A Vallado. *Fundamentals of astrodynamics and applications*. Springer Science & Business Media, 2013.
8. Andrew Vernon Schaeperkoetter. *A comprehensive comparison between angles-only initial orbit determination techniques*. PhD thesis, exas A&M University, 2012.
9. Bob Schutz, Byron Tapley, and George H Born. *Statistical orbit determination*. Elsevier, 2004.
10. Centre National d'Etudes Spatiales (CNES). Patrius library, dedicated to space dynamics tools. <https://www.connectbycnes.fr/patrius>.